Fatigue microcracks that initiate fracture are located near elevated intracortical porosity but not elevated mineralization

Travis L. Turnbull [1], Andrew P. Baumann, Ryan K. Roeder *

Department of Aerospace and Mechanical Engineering, Bioengineering Graduate Program, University of Notre Dame, Notre Dame, IN 46556, USA

ABSTRACT

In vivo microcracks in cortical bone are typically observed within more highly mineralized interstitial tissue, but postmortem investigations are inherently limited to cracks that did not lead to fracture which may be misleading with respect to understanding fracture mechanisms. We hypothesized that the one fatigue microcrack which initiates fracture is located spatially adjacent to elevated intracortical porosity but not elevated mineralization. Therefore, the spatial correlation between intracortical porosity, elevated mineralization, and fatigue microdamage was investigated by combining, for the first time, sequential, nondestructive, three-dimensional micro-computed tomography (micro-CT) measurements of each in cortical bone specimens subjected to compressive fatigue loading followed by a tensile overload to fracture. Fatigue loading resulted in significant microdamage accumulation and compromised mechanical properties upon tensile overload compared to control specimens. The microdamage that initiated fracture upon tensile overload was able to be identified in all fatigue-loaded specimens using contrast-enhanced micro-CT and registered images. Two-point (or pair) correlation functions revealed a spatial correlation between microdamage at the fracture initiation site and intracortical porosity, but not highly mineralized tissue, confirming the hypothesis. This difference was unique to the fracture initiation site. Intracortical porosity and highly mineralized tissue exhibited a significantly lower and higher probability, respectively, of being located spatially adjacent to all sites of microdamage compared to the fracture initiation site. Therefore, the results of this study suggest that human cortical bone is tolerant of most microcracks, which are generally compartmentalized within the more highly mineralized interstitial tissue, but a single microcrack of sufficient size located in spatial proximity to intracortical porosity can compromise fracture resistance.

1. Introduction

Microcracks in cortical bone are typically observed to readily initiate upon repetitive mechanical loading within more highly mineralized interstitial tissue (Schaffler et al., 1995; Norman and Wang, 1997; Diab and Vashishth, 2007; Norman et al., 2008), but arrest at microstructural barriers such as osteons (O'Brien et al., 2003; Mohsin et al., 2006; Kennedy et al., 2008). However, the microarchitectural conditions which allow arrested microcracks to break free of osteons upon continued fatigue loading and/or cause catastrophic fracture upon a single loading event (e.g., fall) are not well understood.

The well-established observation that *in vivo* microcracks are predominantly located within more highly mineralized interstitial tissue, and subsequent attention to these microcracks, may be unintentionally misleading with respect to understanding of fracture mechanisms and fracture risk. Postmortem investigations of these microcracks are inherently limited to cracks that did not lead to a fracture. However, the entire field of fracture mechanics was founded upon Griffith's theory that only one critically-sized flaw, or stress concentration, is necessary for fracture. Thus, identification of the one microcrack that ultimately leads to fracture may be obscured by attention to hundreds of microcracks that do not lead to fracture.

Intracortical porosity is well-known to compromise the mechanical properties of cortical bone (Currey, 1988; Schaffler and Burr, 1988; Yeni et al., 1997; Ural and Vashishth, 2007; Kennedy et al., 2009; Chan and Nicollela, 2012), as would be expected with any engineering material. However, little attention has been given to the interaction of intracortical porosity and fatigue microdamage. The hypothesis that intracortical porosity provides stress concentrations for primary crack initiation, and/or secondary crack initiation ahead of a propagating microcrack, has been largely

* Correspondence to: Department of Aerospace and Mechanical Engineering, Bioengineering Graduate Program, 148 Multidisciplinary Research Building, University of Notre Dame, Notre Dame, IN 46556, USA. Tel.: +1 5 7 4 631 7003; fax: +1 5 7 4 631 2144.
E-mail address: rroeder@nd.edu (R.K. Roeder).
[1] Current Position and Address: Research Engineer, Department of BioMedical Engineering (BME), Steadman Philippon Research Institute (SPRI), 181 W. Meadow Drive, Suite 1000, Vail, CO 81657, USA.

overlooked with a few possible exceptions (Fleck and Eifler, 2003; Soicher et al., 2011; Chan and Nicollela, 2012), perhaps because *in vivo* microcrack density is only weakly correlated with intracortical porosity (Norman et al., 2008). However, as discussed above, the *in vivo* microcrack density is inherently biased and dominated by microcracks that did not lead to fracture.

We hypothesized that fatigue microcracks which initiate fracture are located spatially adjacent to elevated intracortical porosity but not elevated mineralization. Therefore, the objective of this study was to investigate the spatial correlation between intracortical porosity, elevated mineralization, and fatigue microdamage by combining, for the first time, sequential, nondestructive, three-dimensional (3-D) micro-computed tomography (micro-CT) measurements of each in cortical bone specimens subjected to cyclic loading followed by an overload to fracture *in vitro*. Fatigue microdamage was imaged using contrast-enhanced micro-CT with a barium sulfate stain as previously described and validated (Landrigan et al., 2011; Turnbull et al., 2011).

2. Materials and methods

2.1. Specimen preparation

Sixteen femoral cortical bone specimens were prepared from the proximal and mid-diaphysis (Fig. 1) of an 85 year-old male tissue donor presenting no medical history of skeletal pathology or trauma. All tissues were obtained with donor consent (National Disease Research Interchange, Philadelphia, PA) and all protocols were approved by the Notre Dame Human Subjects Institutional Review Board. Two 4.5 cm segments of the diaphysis, centered at 50% and 75% of the total femur length (Fig. 1a), were removed while frozen. Paired specimen blanks were removed from each anatomic quadrant of each section (Fig. 1b) using a low-speed diamond wafer saw (Isomet, Buehler, Lake Bluff, IL). Each specimen blank was kept hydrated with deionized (DI) water while machining into cylindrical "dog-bone" specimens with a 10 mm gauge length and 3 mm gauge diameter (Fig. 1c) using a computer numerical controlled mill and lathe. Paired specimens were randomly divided into a non-loaded control group and a fatigue-loaded group. Specimens were kept hydrated in phosphate buffered saline (PBS) at all times and stored at −20 °C
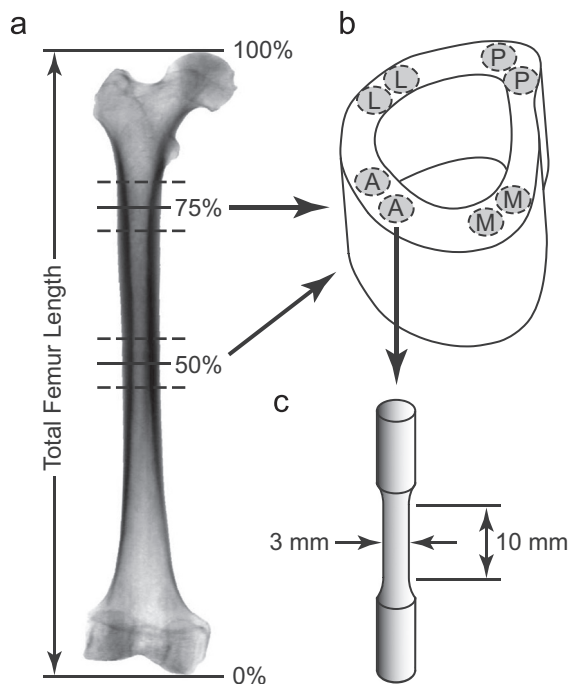
Fig. 1. Paired human cortical bone specimens were sampled from (a) the femoral diaphysis at 50% and 75% of the total femoral length, as shown schematically on a radiograph of the human femur, and (b) each anatomic quadrant (*A*=anterior, *M*=medial, *P*=posterior, and *L*=lateral), and (c) machined into cylindrical specimens with a reduced gauge section.

wrapped in gauze in airtight containers during interim periods. One specimen pair was removed from the study after one specimen fractured during preparation.

2.2. Micro-CT imaging (step 1)

The entire gauge section of each specimen in both the non-loaded control group and fatigue-loaded group was imaged by micro-CT (μCT-80, Scanco Medical AG, Brüttisellen, Switzerland) at each of three sequential steps: (1) as-prepared, (2) after labeling fatigue microdamage, and (3) after fracture due to an overload. Micro-CT images were acquired at 10 μm resolution, 70 kVp voltage, and 114 μA current with 1000 projections at a 600 ms integration time with slices oriented perpendicular to the longitudinal specimen axis. A custom fixture ensured consistent positioning of a specimen for each of the multiple micro-CT scans and expedited subsequent image registration. Noise in grayscale images of as-prepared specimens was reduced using a Gaussian filter (sigma=0.8, support=1). The bone volume (BV) was segmented from the pore volume (PV) (Fig. 2) at a constant global threshold of 270. This threshold value corresponded to ∼840 mg hydroxyapatite per cubic centimeter (mg HA/cm^3) using a custom calibration phantom (Deuerling et al., 2010). Intracortical porosity was reported as the percentage of PV within the total volume (TV=PV+BV). The BV was further segmented into a low mineral level volume (LMV) and a high mineral level volume (HMV) (Fig. 2) corresponding to the lowest 20% and highest 20%, respectively, of voxels within the BV averaged for all specimens. Gaussian filter parameters (sigma=1.5, support=3) and the BV threshold (290, 2.32 cm^{-1}, or ∼920 mg HA/cm^3) were altered for micro-CT measurements at steps (2) and (3) to account for the overall shift in image intensity resulting from barium sulfate stain attenuation and thus segment the same PV as in step (1) (Landrigan et al., 2011). High intensity voxels representative of damaged tissue volume (DV) were segmented at a constant global threshold of 490, corresponding to a mean linear attenuation coefficient of 3.92 cm^{-1} or ∼1890 mg HA/cm^3, which was well above the tissue mineral density of human cortical bone (Deuerling et al., 2010).

### 2.3. Fatigue loading and microdamage labeling (step 2)

Paired specimens were either not loaded (control) or subjected to cyclic uniaxial compression at 2 Hz with a sinusoidal waveform in an ambient PBS bath under load control using an electromagnetic test instrument (ElectroForce 3300, Bose Corp., Eden Prairie, MN). Fatigue-loaded specimens were first preconditioned with a maximum compressive stress of 40 MPa for 240 cycles. Following preconditioning, specimens were subjected to a maximum cyclic compressive stress of 75 MPa (*R*=0.1) in the gauge section until reaching a 10% reduction in secant modulus. The secant modulus degradation during fatigue loading was calculated as the percent reduction in instantaneous secant modulus at a given number of loading cycles relative to the initial secant modulus. The initial secant modulus was defined as the average secant modulus of the first 20 cycles during fatigue loading. The total number of loading cycles was recorded upon reaching the predetermined secant modulus degradation for each specimen.

All specimens were stained by barium sulfate (BaSO$_4$) precipitation to label preexisting microdamage and/or microdamage resulting from fatigue loading using methods previously described and validated (Landrigan et al., 2011; Turnbull et al., 2011). Specimens were imaged again by micro-CT, as described above. The ratio of damage volume to bone volume (DV/BV) was adopted as a measure of microdamage (Landrigan et al., 2011; Turnbull et al., 2011). The gauge section was segmented to reveal labeled microdamage (DV), which was overlaid on micro-CT images of the as-prepared specimens using image registration (Analyze 10.0, Mayo Foundation for Medical Education and Research, Rochester, MN) (Fig. 3).

Non-specific staining of tissue porosity and on exterior specimen surfaces was minimized in a series of three steps. First, the segmented BV of each as-prepared specimen was applied as an inclusion mask to the corresponding segmented DV after registration such that the resulting image volume contained only stain within the bone matrix or BV, not stain within the PV. Second, a MATLAB (v7.14, The MathWorks, Inc., Natick, MA) script was written to eliminate clusters of DV at the specimen free surface which did not penetrate into the specimen interior. At least 25% of the voxels in each DV cluster were required to penetrate the specimen more than 100 μm (10 voxels) from the free surface in order to be included. Last, a 100 μm (10 voxels) peel was applied to the DV to remove non-specific BaSO$_4$ staining on the exterior specimen surface (Landrigan et al., 2011).

2.4. Tensile overload (step 3)

All specimens were hydrated in PBS for 1 h prior to overload, loaded to failure in uniaxial tension at a displacement rate of 25 mm/s, and imaged again by micro-CT as described above. Micro-CT images of fractured specimens were registered with micro-CT images of the as-prepared specimens to identify the fracture initiation site by the presence of labeled DV on the fracture surface of fatigue-loaded specimens (Fig. 4). The elastic modulus (*E*), ultimate tensile strength (*UTS*), strain-to-failure (ε_f), and work of fracture (w_f) were calculated from measured force–displacement data and dimensions of the specimen gauge section using standard methods (Roeder, 2013).
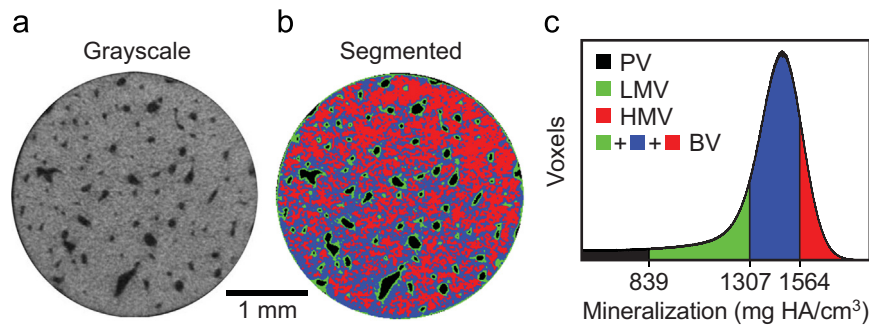
Fig. 2. (a) A representative grayscale micro-CT image for a transverse specimen cross-section, (b) the corresponding segmented micro-CT image, and (c) the corresponding histogram for the entire specimen volume prior to inducing microdamage by fatigue loading, showing the segmentation and distribution of intracortical porosity (PV), as well as the low (LMV) and high (HMV) mineral level volumes within the bone volume (BV).
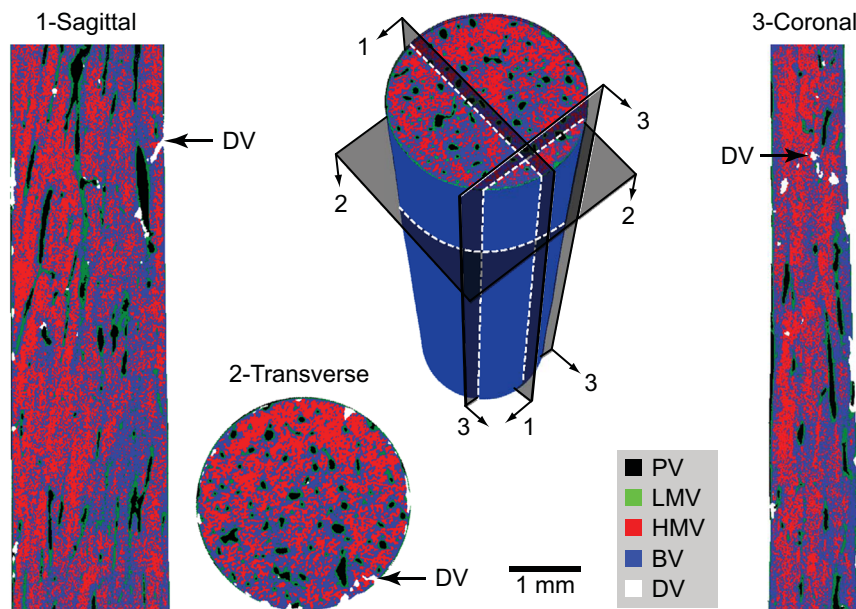
Fig. 3. Segmented, orthogonal micro-CT cross-sections of a representative fatigue-loaded specimen after BaSO$_4$ labeling of fatigue microdamage showing the labeled DV (white, arrows) that was subsequently confirmed to be the site of fracture initiation in close proximity to a large pore. 1=sagittal, 2=transverse, 3=coronal, PV=pore volume, LMV=low mineral level volume, HMV=high mineral level volume, BV=remaining bone volume, DV=damage volume.

2.5. Analytical and statistical methods

The two-point (or pair) correlation function, $g(r)$, for encountering a microstructural feature of interest, B, as a function of the 3-D radial distance, r, from voxels of origin within another microstructural feature, A, was calculated as (Cruz-Orive, 1989; Reed and Howard, 1999; Torquato, 2002),

$$g(r)_{A-B} = \frac{\langle V_B(r) \rangle_A}{V_B} \qquad (1)$$

where B is the feature of interest (e.g., PV, HMV, LMV), $V_B(r)$ is the volume fraction of B within a spherical shell of voxels at distance r from a voxel of origin in A, V_B is the total volume fraction of B in the entire sample space, and $g(r)=1$ corresponds to random probability for encountering B at a distance r from A. Thus, the local volume fraction of a feature of interest (PV, HMV, or LMV) located at each radial distance r from voxels of origin within another feature (DVs or PVs) was normalized by the overall volume fraction of the feature of interest, as illustrated in Appendix A as Supplementary materials. The bounds of $g(r)$ include a minimum value of 0, a maximum value of V_B^{-1}, and $g(r)$ approaches 1 as r increases due to $V_B(r)$ approaching V_B. Thus, the threshold for HMV and LMV (upper and lower 20% of BV, or ~16% of TV) across all specimens was intentionally chosen to be no different than the mean intracortical porosity (19.2%), such that the maximum possible value of $g(r)$ was comparable between HMV, LMV, and PV.

Segmented micro-CT images were imported into MATLAB (v7.14, The MathWorks, Inc., Natick, MA) and two-point correlation functions were calculated using a custom MATLAB script, which is available in Appendix B as Supplementary

materials. Rather than estimate $V_B(r)$ from random sets of points or dipoles (Cruz-Orive, 1989; Reed and Howard, 1999), $V_B(r)$ was calculated and averaged for every possible voxel of origin, or a systematic subset of voxels, within microstructural feature A, where A included either the PV, the DV that initiated fracture, or all DVs (Eq. (1)). A sensitivity analysis assessed sampling all (100%) or a subset (50%, 5%, 0.1%, or 0.01%) of voxels within the DV. Sampling 5% of DV voxels (evenly spaced, e.g., every twentieth voxel) in the gauge section, which was typically on the order of 50,000 DV voxels per specimen, was shown to minimize computational time without compromising accuracy. Therefore, all subsequent two-point correlation functions and those reported herein were calculated by sampling 5% of voxels within microstructural feature A. Computations were performed on 8 processors utilizing 12 GB of memory and required a maximum wall clock computation time of ~15 h per specimen to compute two-point correlation functions for all features of interest.

Two-point correlation functions for each pair of microstructural features were calculated for each specimen, averaged, and plotted as a mean $g(r)$ with a 95% confidence interval. In order to facilitate statistical comparisons, the mean value of $g(r)$ was calculated for encountering PV, HMV, and LMV within the first 440 μm from either the DV that initiated fracture or all DVs. The distance of 440 μm was chosen as a threshold length for cracks to break free of microstructural barriers (Mohsin et al., 2006).

Intracortical porosity (PV/TV), labeled microdamage (DV/BV), and the mechanical properties of fatigue-loaded specimens were compared to non-loaded control specimens using Wilcoxon Signed Rank tests for matched pairs (JMP 10.0, SAS Institute, Cary, NC). DV/BV was correlated with the number of loading cycles using linear least squares regression. Mean $g(r)$ values for PV, HMV, and LMV within the
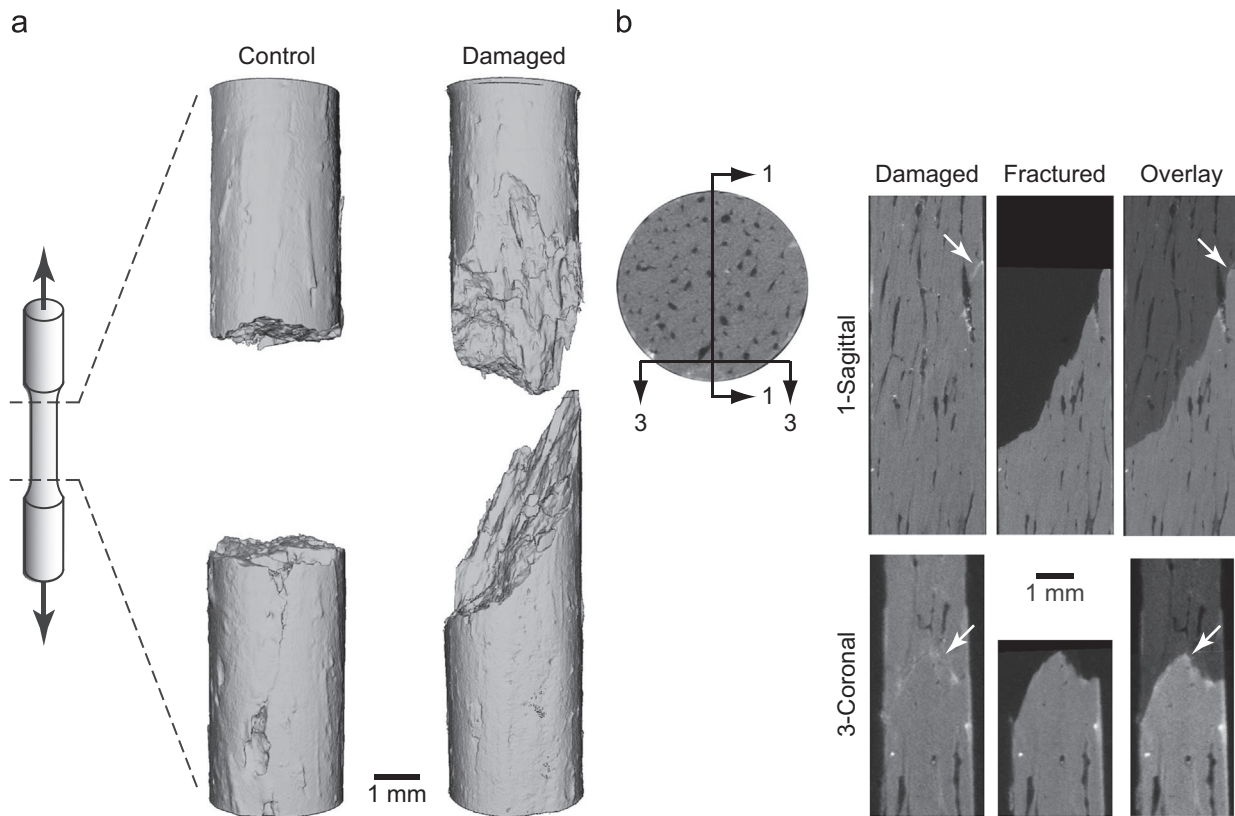
Fig. 4. (a) Segmented micro-CT reconstructions for a representative control and fatigue-loaded specimen after fracturing under a tensile overload and (b) corresponding orthogonal grayscale micro-CT images for the fatigue-loaded specimen before (damaged) and after fracture. The fracture surfaces of fatigue-loaded specimens were tortuous and oblique, corresponding to the labeled fatigue microdamage (DV, bright voxels, arrows), whereas the fracture surfaces of control specimens were transverse and relatively smooth. 1=sagittal, 3=coronal.

first 440 µm from either the DV that initiated fracture or all damage sites (DVs) were compared to random probability ($g(r)=1$) using a Mann–Whitney U-test with a hypothesized mean of 1. Mean $g(r)$ values for each feature of interest (PV, HMV, and LMV) within the first 440 µm from the fracture initiation site versus all damage sites (DVs) were compared using Wilcoxon Signed Rank tests for matched pairs. The level of significance for all tests was set at $p < 0.05$.

3. Results

Segmented, 3-D micro-CT reconstructions of as-prepared (Fig. 2) and fatigue-loaded (Fig. 3) specimens revealed the spatial distribution of intracortical porosity (PV), low and high levels of mineralization (LMV and HMV, respectively), and damage (DV). The mean ($\pm$ standard deviation) intracortical porosity (PV/TV) for all specimens in this study was 19.2 (11.9) vol%; differences between control and fatigue-loaded specimens (Table 1) were not statistically significant ($p=0.80$, Wilcoxon Signed Rank). HMV was observed to be heterogeneously distributed within the BV in between PVs, corresponding to expected locations of interstitial tissue (Figs. 2 and 3). The two-point correlation function, $g(r)$, confirmed that the likelihood of HMV located at radial distances from intracortical porosity (PV) was much less than random probability near PVs and increased to random probability with increased distance away from PVs (Fig. 5). LMV appeared to be located in close spatial proximity to PVs (Figs. 2 and 3), as expected of osteonal tissue surrounding Haversian canals. The two-point correlation function, $g(r)$, confirmed that the likelihood of LMV located at radial distances from intracortical porosity (PV) was greater than random probability near PVs, specifically within the first ~ 200 µm, and decreased to random probability with increased distance away from PVs (Fig. 5). Overall, labeled damage (DV) appeared at random locations with

respect to the macroscopic gauge section and across all specimens. However, the largest regions of DV in each individual specimen appeared to be located in proximity to locally elevated intracortical porosity (PV) and/or the specimen free surface (Fig. 3).

Fatigue-loaded specimens exhibited significantly increased levels of labeled microdamage (DV/BV) compared to non-loaded control specimens ($p < 0.05$, Wilcoxon Signed Rank) (Table 1). The number of loading cycles required to reach a 10% reduction in secant modulus for fatigue-loaded specimens was highly variable (Table 1), as expected, and DV/BV was therefore not correlated with the number of fatigue loading cycles ($p > 0.25$). The level of microdamage accumulated in fatigue specimens was sufficient to significantly compromise the mechanical properties upon a tensile overload to failure compared to control specimens (Table 1). Fatigue-loaded specimens exhibited $\sim 30\%$ reduction in elastic modulus, $\sim 65\%$ reduction in ultimate tensile strength, $\sim 55\%$ reduction in strain-to-failure, and $\sim 85\%$ reduction in work of fracture ($p < 0.05$, Wilcoxon Signed Rank), compared to non-loaded control specimens (Table 1).

All fatigue-loaded specimens exhibited a tortuous oblique fracture surface upon tensile overload (Fig. 4a) due to the presence of predominately longitudinal microcracks (DV) previously initiated in cyclic compression, often noticeably adjacent to intracortical porosity (PV) (Fig. 4b). Additional grayscale micro-CT images from multiple fatigue-loaded specimens are available in Appendix C as Supplementary materials to show that the loading protocol produced primarily longitudinal microcracks which were labeled by the barium sulfate stain. In contrast, non-loaded control specimens exhibited relatively smooth transverse fracture surfaces (Fig. 4a). The DV that initiated fracture was able to be clearly identified by the presence of a single labeled DV on the fracture surface of all seven

Table 1
The mean (± standard deviation) intracortical porosity (PV/TV), number of fatigue cycles, labeled microdamage (DV/BV), and mechanical properties upon a tensile overload to failure for fatigue-loaded specimens compared to non-loaded control specimens. Tensile overload mechanical properties included the elastic modulus (E), ultimate tensile strength (UTS), strain-to-failure (ε_f), and work of fracture (w_f).

| Group	PV/TV (vol%)	Fatigue Cycles	DV/BV (vol%)	Tensile Overload Mechanical Properties			
				E (GPa)	UTS (MPa)	ε_f (%)	w_f (N-mm)
Control	18.1 (12.2)	0	0.3 (0.2)	7.0 (0.7)	90 (26)	1.9 (0.6)	74 (37)
Fatigue	20.3 (12.4)	24,000 (39,000)	1.4 (1.1)*	5.0 (2.1)*	33 (17)*	0.9 (0.4)*	12 (9)*

* $p < 0.05$ vs. Control, Wilcoxon Signed Rank.
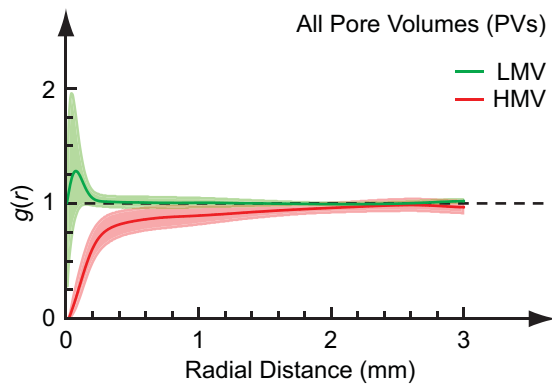
Fig. 5. The two-point correlation function, $g(r)$, for low mineral level volume (LMV) and high mineral level volume (HMV) at radial distances away from all pore volumes (PVs) of intracortical porosity for fatigue-loaded specimens showing the mean (trace) and 95% confidence interval (shading) for $g(r)$. Note that $g(r)=1$ corresponds to random probability.

fatigue loaded specimens (Fig. 4b, arrows). The DV identified with the fracture initiation site also exhibited a size greater than the 97th percentile of all DVs in a specimen rank ordered by volume. In contrast, the fracture surface of all seven non-loaded control specimens contained no labeled DV.

The two-point correlation function, $g(r)$, for all fatigue-loaded specimens revealed a greater than random probability for PV located spatially adjacent to the DV that initiated fracture and a less than random probability for HMV located spatially adjacent to the DV that initiated fracture, before both approached random probability at large distances, as expected (Fig. 6a). This difference was unique to the DV that initiated fracture as PV exhibited a significantly lower probability and HMV exhibited a significantly higher probability of being located adjacent to all damage sites (DVs) (Fig. 6b) compared to only the DV that initiated fracture (Fig. 6a). Note that particularly within the first ~100 μm of all DVs, $g(r)$ for HMV was greater than one while $g(r)$ for PV was much less than one.

In fatigue-loaded specimens, the mean value of $g(r)$ for PV and HMV within a radial distance of 440 μm from the DV that initiated fracture was significantly greater than random probability ($p < 0.05$, Mann–Whitney) and less than random probability ($p < 0.05$, Mann–Whitney), respectively (Fig. 7). In contrast, the mean value of $g(r)$ for either PV ($p=0.08$, Mann–Whitney) or HMV ($p=0.38$, Mann–Whitney) within a radial distance of 440 μm from all damage sites (DVs) was not statistically different from random probability. The mean value of $g(r)$ for PV near the fracture initiation site was significantly greater than that for all damage sites (DVs) ($p < 0.05$, Wilcoxon Signed Rank) (Fig. 7). In contrast, the mean value of $g(r)$ for HMV near the fracture initiation site was significantly less than that for all damage sites (DVs) ($p < 0.05$, Wilcoxon Signed Rank). The mean value of $g(r)$ for LMV located within a radial distance of 440 μm from either the DV that
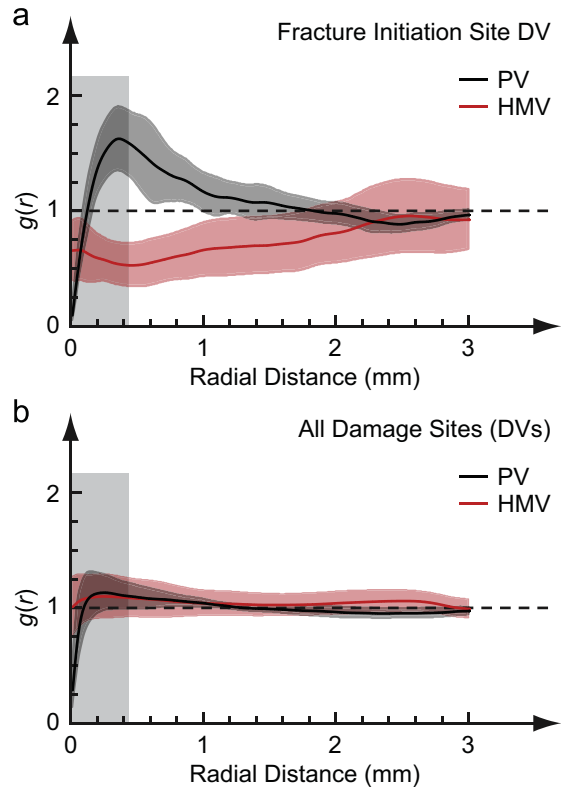
Fig. 6. The two-point correlation function, $g(r)$, for intracortical porosity (PV) and high mineral level volume (HMV) at radial distances away from (a) the fracture initiation site DV or (b) all damage sites (DVs) for all fatigue-loaded specimens showing the mean (trace) and 95% confidence interval (shading) for $g(r)$. Note that $g(r)=1$ corresponds to random probability. Inter-specimen variability in $g(r)$ is shown in Appendix D as Supplementary materials. The radial distance of 440 μm used for Fig. 7 is shown shaded gray.
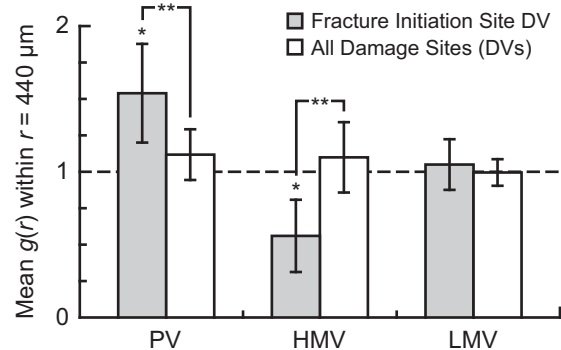
Fig. 7. The mean value of the two-point correlation function, $g(r)$, for intracortical porosity (PV), high mineral level volume (HMV), and low mineral level volume (LMV) within a radial distance of 440 μm from either the fracture initiation site DV or all damage sites (DVs). Note that $g(r)=1$ corresponds to random probability. *$p < 0.05$, Mann–Whitney vs. 1. **$p < 0.05$, Wilcoxon Signed Rank.

initiated fracture or all damage sites (DVs) was not statistically different from random probability ($p=0.47$ and 0.81, respectively, Mann–Whitney) (Fig. 7).

In non-loaded control specimens, the mean value of $g(r)$ for both PV and HMV located within a radial distance of 440 μm from all damage sites (DVs) was significantly greater than random probability ($p < 0.05$, Mann–Whitney), while the mean value of $g(r)$ for LMV was not significantly different from random probability ($p=0.81$, Mann–Whitney).

4. Discussion

Microdamage (DV) at the fracture initiation site was spatially correlated with intracortical porosity (PV), but not highly mineralized tissue (HMV) (Fig. 6a and Fig. 7). This suggests that cortical bone fractures initiated at fatigue microcracks located near elevated intracortical porosity but not elevated mineralization. In contrast, PV exhibited a significantly lower probability and HMV exhibited a significantly higher probability of being located spatially adjacent to all sites of microdamage compared to the fracture initiation site (Figs. 6 and 7). This result suggests that fatigue microcracks readily and stochastically initiated and accumulated primarily within the more highly mineralized interstitial tissue of cortical bone. Taken together, these results suggest that human cortical bone is largely tolerant of microcracks, which are generally compartmentalized within the interstitial tissue (Schaffler et al., 1995; Norman and Wang, 1997; Diab and Vashishth, 2007) and serve to dissipate strain energy (Reilly and Currey, 2000). However, a single microcrack of sufficient size located in spatial proximity to intracortical porosity can compromise fracture resistance.

In fracture mechanics, the stress intensity factor (K) of a microcrack in close proximity to a pore can be solved using the principle of superposition as the sum of the individual components, $K_{total}=K_{microcrack}+K_{pore}$ (Anderson, 2005). Therefore, an increase in the volume fraction or size of intracortical pores (e.g., resulting from metabolic bone disease or transient remodeling to repair microdamage) leads to an increased probability of proximity between a pore and a stochastically generated microcrack. The prediction of fracture risk could thus be improved by clinical assessment of intracortical porosity, which may, in turn, influence pharmacological treatment strategies.

Clinical assessment of fracture risk currently relies upon measuring the projected bone mineral density (BMD) using dual-energy X-ray absorptiometry. BMD is predictive of fracture risk but not without well-documented limitations. About one-half of fractures occur in patients with BMD above the threshold for clinical diagnosis of osteoporosis, and other risk factors (e.g., age) can predict fractures independently of BMD (Siris, et al., 2001; Sornay-Rendu et al., 2005; Sanders et al., 2006). One reason for the lack of sensitivity is that BMD is an aggregate measure that does not differentiate architectural porosity and tissue mineralization (Kazakia et al., 2011). Recent advances in high-resolution peripheral quantitative computed-tomography (HR-pQCT) have enabled 3-D, non-invasive imaging of intracortical porosity at appendicular skeletal sites in vivo (MacNeil and Boyd, 2008; Burghardt et al., 2010a; Liu et al., 2010). Intracortical porosity measured by HR-pQCT in the distal radius and tibia was correlated with age for both men and women, and micro-finite element analysis revealed a significantly greater biomechanical deficit due to intracortical porosity for postmenopausal women relative to premenopausal women (Burghardt et al., 2010b). Therefore, new strategies for fracture risk assessment could be based on directly measured characteristics of intracortical porosity.

The net benefit of bisphosphonate treatment for osteoporosis has been an on-going subject of debate in the literature (Seeman, 2009; Allen and Burr, 2011). The suppression of remodeling by bisphosphonates preserves cortical bone mass, or limits further increases in intracortical porosity, in order to maintain the mechanical integrity of cortical bone (Burghardt et al., 2010c; Allen and Burr, 2011). On the other hand, long term suppression of bone remodeling by bisphosphonates may increase mineralization levels resulting in more brittle tissue and an increased risk of "atypical" fractures (Lenart et al., 2008). The results of this study suggest that the net benefit of limiting increases in intracortical porosity should outweigh the net deficit due to increased mineralization since fracture initiation sites were spatially associated with intracortical porosity but not elevated mineralization. Furthermore, the methods of analysis in this study provide a means to decouple and quantitatively compare the net effects of pharmacological treatments on fracture susceptibility.

The spatial proximity of PV from the fracture initiation site reached maximum probability, $g(r)$, at ~400 μm on average (390 ± 60 μm) (Fig. 6a). This result adds further support to the concept of a critical length of microcracks, which was previously suggested to be 440 μm (Mohsin et al., 2006). Bone permits microcrack initiation but resists crack propagation (Reilly and Currey, 2000; O'Brien et al., 2003). However, there is a limit to the ability of any material to resist crack propagation which coincides with a critical crack length above which a crack possesses enough surface free energy to undergo unstable propagation to failure, in spite of microstructural barriers to crack growth (e.g., osteons and cement lines). Therefore, the mean value of $g(r)$ for PV and HMV within a radial distance of 440 μm from microdamage (DV) was computed for all loaded specimens.

The radial distance of 440 μm was useful and appropriate for testing the fracture hypothesis of this study, but may not be the most appropriate distance for testing other hypotheses. For example, Fig. 7 shows a near random probability of HMV and PV located adjacent to all DVs, which might seem to contradict the well-known histological observation that microcracks are primarily located within the more highly mineralized interstitial tissue. However, 440 μm is too large a distance to test the hypothesis that HMV is spatially correlated with all DVs. Fig. 6b shows that within the first ~100 μm of all DVs, $g(r)$ for HMV was greater than one while $g(r)$ for PV was much less than one. Osteons have been reported to exhibit a mean diameter of ~200 μm in human femoral cortical bone (Britz et al., 2009). Therefore, microcracks or DVs within interstitial bone, which typically arrest at cement lines, would be expected to be located at least ~100 μm away from the nearest PV and within ~100 μm of HMV, as shown in Fig. 6b. Therefore, the results in this study support the well-known histological observation that most microcracks form within the more highly mineralized interstitial tissue.

The computational demand required to calculate $g(r)$ for a single voxel of origin was only ~90 s on a standard laptop, but increased in proportion with the number of voxels of origin. For example, a typical fatigue loaded specimen containing ~1 million DV voxels required ~11 d to compute $g(r)$ for all DVs. Therefore, several measures were taken to improve the computational efficiency. First, since specimens were 3 mm in diameter, the sampling volume was restricted to a 3 mm radius from each individual voxel of origin, such that voxels located more than 3 mm away from a voxel of origin were excluded from the analysis. Next, a pilot study assessed the feasibility of sampling all (100%) or a subset (50%, 5%, 0.1%, or 0.01%) of voxels in the DV. There was no qualitative difference in the mean $g(r)$ and no statistical difference in the mean value of $g(r)$ within a radial distance of 440 μm from the DV ($p < 0.05$, Wilcoxon Signed Rank) when sampling every (100%), every other (50%), or every twentieth (5%) voxel in the DV. However, sampling less than 5% of the voxels in the

DV altered $g(r)$ and was therefore concluded to be an insufficient sampling volume. Sampling 5% of voxels in the DV required a maximum computation time of ~15 h per specimen to compute $g(r)$ for all features of interest.

The threshold for HMV and LMV (upper and lower 20% of BV, or ~16% of TV) across all specimens was intentionally chosen to be no different than the mean intracortical porosity (19.2%), such that the maximum possible value of $g(r)$ was comparable between HMV, LMV, and PV. Nonetheless, a sensitivity analysis was also conducted for the highly mineralized tissue (HMV) threshold, investigating the highest 20% of voxels in the BV compared to the highest 5% of voxels. Restricting HMV voxels to include only the highest 5% within the BV increased noise in $g(r)$ due to the reduced sampling rate, but the mean value of $g(r)$ for HMV within a radial distance of 440 μm from either the DV that initiated fracture or all damage sites (DVs) was not significantly different compared to including the highest 20% of voxels ($p > 0.38$ or 0.55, respectively, Wilcoxon Signed Rank). This result provided additional confidence in the methods for the mineralization threshold and the calculation of $g(r)$.

Several limitations in this study are worth noting. First, this study was limited to a small number of specimens from a single donor, and all measurements were performed *in vitro*. Second, fatigue loading to a 10% reduction in secant modulus produced relatively large microcracks. Moreover, the 30% reduction in modulus upon the tensile overload for fatigue-loaded specimens compared to non-loaded control specimens was a static measure of modulus, and should not be directly compared to the 10% reduction in dynamic modulus during cyclic loading. Third, the DV that initiated fracture was manually selected upon inspection of registered micro-CT images before and after the tensile overload to failure but could be automated in the future. Last, a tensile overload was used to preserve intact fracture surfaces since a compressive overload would damage fracture surfaces and hinder attempts to locate the fracture initiation site. Nonetheless, the novel methods employed in this study facilitated important new insights in the understanding of cortical bone fracture mechanisms and are well-suited for use in future studies investigating fracture susceptibility.

Conflict of interest statement

Funding sources

Acknowledgments

Appendix A. Supplementary material

Supplementary data associated with this article can be found in the online version at http://dx.doi.org/10.1016/j.jbiomech.2014.06.022.

References

Allen, M.R., Burr, D.B., 2011. Bisphosphonate effects on bone turnover, micro-damage, and mechanical properties: what we think we know and what we know that we don't know. Bone 49, 56–65.

Anderson, T.L., 2005. Fracture Mechanics: Fundamentals and Applications, third ed. CRC Press, Boca Raton, FL.

Britz, H.M., Thomas, C.D.L., Clement, J.G., Cooper, D.M.L., 2009. The relation of femoral osteon geometry to age, sex, height and weight. Bone 45, 77–83.

Burghardt, A.J., Buie, H.R., Laib, A., Majumdar, S., Boyd, S.K., 2010a. Reproducibility of direct quantitative measures of cortical bone microarchitecture of the distal radius and tibia by HR-pQCT. Bone 47, 519–528.

Burghardt, A.J., Kazakia, G.J., Ramachandran, S., Link, T.M., Majumdar, S., 2010b. Age- and gender-related differences in the geometric properties and biomechanical significance of intracortical porosity in the distal radius and tibia. J. Bone Miner. Res. 25, 983–993.

Burghardt, A.J., Kazakia, G.J., Sode, M., de Papp, A.E., Link, T.M., Majumdar, S., 2010c. A longitudinal HR-pQCT study of alendronate treatment in postmenopausal women with low bone density: relations among density, cortical and trabecular microarchitecture, biomechanics, and bone turnover. J. Bone Miner. Res. 25, 2558–2571.

Chan, K.S., Nicolella, D.P., 2012. Micromechanical modeling of R-curve behaviors in human cortical bone. J. Mech. Behav. Biomed. Mater. 16, 136–152.

Cruz-Orive, L.M., 1989. Second-order stereology: estimation of second moment volume measures. Acta Stereol. 8, 641–646.

Currey, J.D., 1988. The effect of porosity and mineral content on the Young's modulus of elasticity of compact bone. J. Biomech. 21, 131–139.

Deuerling, J.M., Rudy, D.J., Niebur, G.L., Roeder, R.K., 2010. Improved accuracy of cortical bone mineralization measured by polychromatic microcomputed tomography using a novel high mineral density composite calibration phantom. Med. Phys. 37, 5138–5145.

Diab, T., Vashishth, D., 2007. Morphology, localization and accumulation of in vivo microdamage in human cortical bone. Bone 40, 612–618.

Fleck, C., Eifler, D., 2003. Deformation behaviour and damage accumulation of cortical bone specimens from the equine tibia under cyclic loading. J. Biomech. 36, 179–189.

Kazakia, G.J., Burghardt, A.J., Link, T.M., Majumdar, S., 2011. Variations in morphological and biomechanical indices at the distal radius in subjects with identical BMD. J. Biomech. 44, 257–266.

Kennedy, O.D., Brennan, O., Mauer, P., Rackard, S.M., O'Brien, F.J., Taylor, D., Lee, T.C., 2008. The effects of increased intracortical remodeling on microcrack behaviour in compact bone. Bone 43, 889–893.

Kennedy, O.D., Brennan, O., Rackard, S.M., Staines, A., O'Brien, F.J., Taylor, D., Lee, T.C., 2009. Effects of ovariectomy on bone turnover, porosity, and biomechanical properties in ovine compact bone 12 months postsurgery. J. Orthop. Res. 27, 303–309.

Landrigan, M.D., Li, J., Turnbull, T.L., Burr, D.B., Niebur, G.L., Roeder, R.K., 2011. Contrast-enhanced micro-computed tomography of fatigue microdamage accumulation in human cortical bone. Bone 48, 443–450.

Lenart, B.A., Lorich, D.G., Lane, J.M., 2008. Atypical fractures of the femoral diaphysis in postmenopausal women taking alendronate. N. Engl. J. Med. 258, 1304–1306.

Liu, X.S., Zhang, X.H., Sekhon, K.K., Adams, M.F., McMahon, D.J., Bilezikian, J.P., Shane, E., Guo, X.E., 2010. High-resolution peripheral quantitative computed tomography can assess microstructural and mechanical properties of human distal tibial bone. J. Bone Miner. Res. 25, 746–756.

MacNeil, J.A., Boyd, S.K., 2008. Bone strength at the distal radius can be estimated from high-resolution peripheral quantitative computed tomography and the finite element method. Bone 42, 1203–1213.

Mohsin, S., O'Brien, F.J., Lee, T.C., 2006. Osteonal crack barriers in ovine compact bone. J. Anat. 208, 81–89.

Norman, T.L., Little, T.M., Yeni, Y.N., 2008. Age-related changes in porosity and mineralization and in-service damage accumulation. J. Biomech. 41, 2868–2873.

Norman, T.L., Wang, Z., 1997. Microdamage of human cortical bone: incidence and morphology in long bones. Bone 20, 375–379.

O'Brien, F.J., Taylor, D., Lee, T.C., 2003. Microcrack accumulation at different intervals during fatigue testing of compact bone. J. Biomech. 36, 973–980.

Reed, M.G., Howard, C.V., 1999. Stereological estimation of covariance using linear dipole probes. J. Microsc. 195, 96–103.

Reilly, G.C., Currey, J.D., 2000. The effects of damage and microcracking on the impact strength of bone. J. Biomech. 33, 337–343.

Roeder, R.K., 2013. Mechanical characterization of biomaterials. In: Bandyopadhyay, A., Bose, S. (Eds.), Characterization of Biomaterials. Elsevier, Waltham, MA, pp. 49–104.

Sanders, K.M., Nicholson, G.C., Watts, J.J., Pasco, J.A., Henry, M.J., Kotowicz, M.A., Seeman, E., 2006. Half the burden of fragility fractures in the community occur in women without osteoporosis. When is fracture prevention cost-effective? Bone 38, 694–700.

Schaffler, M.B., Burr, D.B., 1988. Stiffness of compact bone: effects of porosity and density. J. Biomech. 21, 13–16.

Schaffler, M.B., Choi, K., Milgrom, C., 1995. Aging and matrix microdamage accumulation in human compact bone. Bone 17, 521–525.

Seeman, E., 2009. To stop or not to stop, that is the question. Osteoporos. Int. 20, 187–195.

Siris, E.S., Miller, P.D., Barrett-Connor, E., Faulkner, K.G., Wehren, L.E., Abbott, T.A., Berger, M.L., Santora, A.C., Sherwood, L.M., 2001. Identification and fracture outcomes of undiagnosed low bone mineral density in postmenopausal women. J. Am. Med. Assoc. 286, 2815–2822.

Soicher, M.A., Wang, X., Zauel, R.R., Fyhrie, D.P., 2011. Damage initiation sites in osteoporotic and normal human cancellous bone. Bone 48, 663–666.

Sornay-Rendu, E., Munoz, F., Garnero, P., DuBoeuf, F., Delmas, P.D., 2005. Identification of osteopenic women at high risk of fracture: the OFELY study. J. Bone Miner. Res. 20, 1813–1819.

Torquato, S., 2002. Random heterogeneous materials: microstructure and macroscopic properties. In: Antman, S.S., Marsden, J.E., Sirovich, L., Wiggins, S. (Eds.), Interdisciplinary Applied Mathematics. Springer-Verlag, New York, NY.

Turnbull, T.L., Gargac, J.A., Niebur, G.L., Roeder, R.K., 2011. Detection of fatigue microdamage in whole rat femora using contrast-enhanced micro-computed tomography. J. Biomech. 44, 2395–2400.

Ural, A., Vashishth, D., 2007. Effects of intracortical porosity on fracture toughness in aging human bone: a μCT-based cohesive finite element study. J. Biomech. Eng. 129, 625–631.

Yeni, Y.N., Brown, C.U., Wang, Z., Norman, T.L., 1997. The influence of bone morphology on fracture toughness of the human femur and tibia. Bone 21, 453–459.